

Myofibroblasts slow down defect recombination dynamics in mixed cell monolayers

Zhaofei Zheng¹, Yuxin Luo¹, Juan Chen^{1,2}, and Yimin Luo^{1,*}

¹Department of Mechanical Engineering, Yale University, New Haven, CT

²Current address: University of Maryland Medical Center, Baltimore, MD

*Corresponding author: yimin.luo@yale.edu

Abstract

Cellular organization and mechanotransduction pathways are crucial regulators of tissue morphogenesis, whereas their dysregulation contributes to pathologies. Overactive fibroblasts, or myofibroblasts, are key drivers of fibrosis, yet how their presence alters collective cellular ordering remains unclear. Inspired by the analogy between liquid crystals and cells, we investigate how topological defects influence reorganization in dense monolayers of co-cultured fibroblasts and myofibroblasts. Owing to steric interactions, these elongated cells exhibit local order; topological defects, where alignment is disrupted, have been postulated to serve as mechanical centers. In this study, we examine how the incorporation of contractile myofibroblasts impacts defect relaxation. The behavior is reminiscent of active nematics with quenched disorder: myofibroblast concentration modulates the disorder strength; increasing their fraction slows defect recombination. Higher myofibroblast concentrations similarly reduce the overall cell alignment on microgrooved surfaces, as myofibroblasts interfere with monolayer reorganization. This observation highlights the potential of a simple, quantitative assay for diagnosing disease progression. Furthermore, we found that myofibroblasts preferentially localize at negatively charged $-\frac{1}{2}$ defects, compared to fibroblasts, which tend to be localized in $+\frac{1}{2}$ defects. Consequently, the slowdown of recombination dynamics can be partially attributed to the reduced velocity of the more mobile $+\frac{1}{2}$ defects. Our study suggests that myofibroblasts can exploit negatively charged defects by avoiding regions of compressive stress and evading apoptosis. Combining live-cell imaging and immunofluorescence studies, this work provides insights into the role of topological defects in fibrotic disease progression.

Keywords: topological defects, active nematics, mechanotransduction, myofibroblasts

1 Introduction

Liquid crystals (LCs) underlie technological advancement, exemplified by LC displays. Many biological systems, from cytoskeletons to lipid bilayers [1, 2], also exhibit an LC phase. A growing body of literature draws parallels between cell ordering and LCs, where the orientation of an individual cell is represented by a headless vector (the “director”), and steric interaction between cells causes them to co-align [3–6]. In addition, cells also align parallel with physical boundaries [7, 8], akin to LC anchoring, and exhibit deformations analogous to classical splay and bend modes [9]. As density increases, elongated cells undergo a disorder-to-order transition [10], suggesting a collective mechanism for sensing substrate anisotropy. At high densities, the system jams, and both reorientation and proliferation cease [11].

Cell alignment is typically imperfect in a monolayer; the order can be quantified by the order parameter S , which ranges from 0 (random) to 1 (perfect alignment). Cell movements naturally engender topological defects, areas within cell assemblies where order is disrupted or frustrated ($S = 0$). In 2D, defects are characterized by a topological “charge” measuring the angle by which the director field rotates as one encircles the defect. Originally considered an academic novelty, defects were later found to play a key role in tissue maintenance, and their movement can provide insights into the nature of the underlying forces [5, 12, 13]. Over time, cells accumulate at $+\frac{1}{2}$ defects and depleted at $-\frac{1}{2}$ defects. As a result, cells can eventually form mounds at $+\frac{1}{2}$ defects [5], and elevated rates of cell apoptosis and extrusion

due to compressive stresses concentrating at those sites [12]. This analogy could even be extended to 3D, paving the way for controlled force generation and shape transformation [14, 15]. Perhaps most strikingly, topology-driven morphogenesis can operate at the scale of entire organisms; a well-known example is the role of topological defects in establishing a robust body plan in Hydra [16].

LC orders have been uncovered in an ever-growing list of cell types [17], from muscle cells [18] and breast cancer cells [12], to retinal cell lines [19]. While the LC ordering in cells is now well-recognized, leveraging the active nematics framework to gain insights into development and disease progression remains a recent and rapidly emerging area of research. Topological defects have been shown to guide the self-assembly of stromal cells into cartilage tissues [20]. In the mesothelial layer, defects direct tissue flow, with regions of net inward flow inhibiting tumor cell clearance [21]. Aligned layers of cancer-associated fibroblasts act as defensive barriers, whereas topological defects represent weak spots that can be exploited for cancer cell dissemination [22]. More recently, brain cancer cells (gliomas) have been found to exhibit large-scale ordering, with the degree of this organization correlating to the tumor aggressiveness [23, 24].

One underexplored context is how the LC order is mediated in a system that consists of two distinct cell phenotypes. Phenotype refers to organisms with the same genetic composition, but exhibiting different physical characteristics owing to their interaction with environmental factors. For example, when fibroblasts, the connective tissue cells, encounter stiff environments [25, 26] or chemical signals [27], they turn into a strongly contractile phenotype, myofibroblasts, to facilitate wound healing. However, myofibroblasts are also known drivers for fibrosis [28]. During normal tissue healing, activated myofibroblasts help close the wound, but undergo apoptosis, or programmed cell death, once the wound closes [29]. However, during fibrotic disease progression, the activated myofibroblasts surprisingly evade apoptosis [30]. While single-cell force profiling and fluorescence staining can provide valuable insights [31], they may not fully capture the complexity of these multicellular dynamics due to their limited sample size and static nature. Physiological activities such as wound healing, maintenance, and morphogenesis require coordinated force generation and typically emerge collectively from a heterogeneous population. This is also the reason why the loss of tissue organization often indicates underlying inflammatory conditions [32]. Nonetheless, it remains unclear how the fraction of myofibroblasts in the population influences the dynamics of monolayer organization. There is an unmet need for simplified, predictive *in vitro* models that can clarify the mechanisms linking cell phenotypes to tissue organization and enable quantitative monitoring of fibrosis without sampling-related biases.

In this work, we create an *in vitro* system consisting of fibroblasts and myofibroblasts of varying ratios to mimic the progressive nature of fibrosis. Using time-lapse live-cell microscopy and immunofluorescence, we study topological defects that arise naturally in dense monolayers and when cells are cultured on topographically patterned substrates. Our study reveals the following: 1) Myofibroblasts adopt an elongated morphology in response to surrounding fibroblasts. Together, these two phenotypes form an active nematic layer, where elasticity dominates over activity. 2) Defect relaxation slows down with increasing myofibroblast concentration, reminiscent of systems with quenched disorder, with the myofibroblast fraction acting as a tunable disorder strength. 3) Using a substrate with unidirectional orientation, we demonstrate that monolayers containing more myofibroblasts exhibit decreased alignment order, thereby establishing external alignment as a quantitative diagnostic platform for monitoring the amount of myofibroblasts in the system. 4) Distinct phenotypes develop affinity for defects of different topological charges. Less active myofibroblasts exploit defects in long-range LC organization by avoiding the more motile, positively-charged defects. Together, these findings suggest that defects create a distinct mechanical environment and illuminate the feedback loop between defect stabilization and local myofibroblast enrichment.

2 Results

2.1 Tracking defect dynamics in progressive disease model

To characterize typical dermal compositions, dermal biopsy samples were obtained from healthy donors and individuals with systemic sclerosis (SSc, more details can be found in Supplementary Information, SI, Section S1), where fibrosis is a key symptom. Immunofluorescence staining of tissue samples from patients with SSc shows more activated myofibroblasts compared to a healthy control (Fig. S1a). The biomarker α -SMA is overexpressed in patients with fibrotic disease, while remaining largely absent in

healthy donors. We estimate that cells expressing α -SMA could be as high as 50-70% in SSc patients (Fig. S1b). Their presence can impair dermal function, causing joint stiffness and increased scarring. In dense layers, however, the two phenotypes are difficult to distinguish based on morphology alone, and their mixed presence and proximity suggest their ongoing crosstalk during fibrotic disease progression.

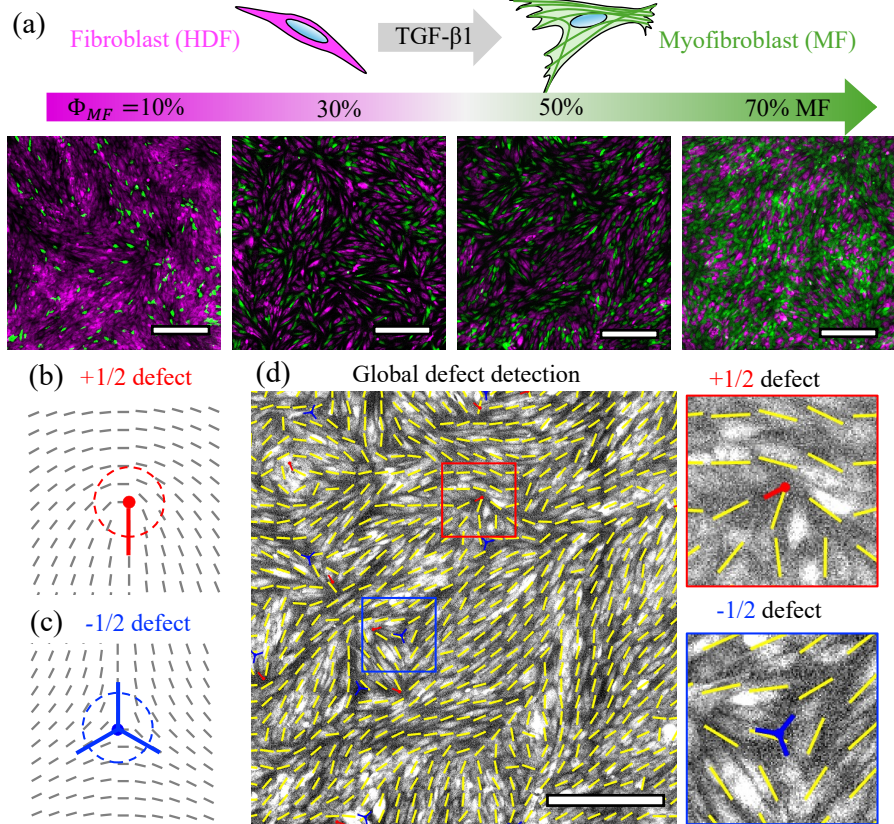


Figure 1: (a) Fluorescent micrographs of mixed fibroblast (magenta) and myofibroblast (green) monolayers, where the percentage of myofibroblasts is systematically increased, mimicking the progression of fibrotic diseases. The scale bars are $500 \mu\text{m}$. (b-c) Schematics of topological defects with charges $\pm \frac{1}{2}$. (d) Defect detection in a real tissue monolayer, where the detected director field is plotted as an overlay in yellow, the cores of the defects are denoted in red ($+\frac{1}{2}$ defects) and blue ($-\frac{1}{2}$ defects), respectively. The inset shows a zoomed-in view of both types of defects. The scale bars are $500 \mu\text{m}$.

To better isolate and control myofibroblast concentration in the sample, we construct a simplified *in vitro* model with mixed phenotypes to mimic progressive disease states. We induce myofibroblasts (MFs) *in vitro* (Fig. 1a and Fig. S2) from adult human dermal fibroblasts (HDFs), by adding transforming growth factor- β 1 (TGF- β 1, 10 ng/mL), a key mediator released by platelets during wound healing, to mimic the chemical environment at the wound site. Both induced and untreated cells retain their phenotypes in media with a reduced concentration of TGF- β 1 (2 ng/mL, Fig. S2). After labeling, the induced cells are counted and mixed with untreated fibroblasts. This procedure results in a well-defined fibroblast (magenta) to myofibroblast (green) ratio, and each phenotype is distinguished by different channels (Fig. 1a). Throughout this study, we avoid using DAPI for live cell imaging to minimize its detrimental effects on the cells. DAPI staining is only used after cell fixation for easier segmentation. We quantify the fraction of myofibroblasts, Φ_{MF} , using three independent approaches in experiments: cell segmentation with Cellpose, nucleus detection using TrackMate, or estimation from the areal fraction after binarizing individual channels. All three methods yield comparable Φ_{MF} (see Section S3 and Fig. S3 for details).

At high density ($\rho_{\text{cell}} \approx 750 \text{ cells mm}^{-2}$), the monolayer behaves as a relaxing solid, exhibiting long-range, correlated motion (Videos S1). In contrast, at lower concentrations ($\rho_{\text{cell}} \approx 500 \text{ cells mm}^{-2}$), individual cells move back and forth without coherent dynamics (Videos S2). Particle image velocimetry (PIV) and velocity correlation (Section S4 and Fig. S4) reveal that monolayers at $\rho_{\text{cell}} \approx 500 \text{ cells mm}^{-2}$ have a velocity correlation length comparable to a single cell ($\approx 100 \mu\text{m}$). On the other hand, at

$\rho_{\text{cell}} \approx 750 \text{ cells mm}^{-2}$, the velocity correlation length increases substantially to hundreds of μm . We are primarily interested in how embedding myofibroblasts affects global relaxation dynamics. Thus, we focus on $\rho_{\text{cell}} \approx 750 \text{ cells mm}^{-2}$ in the subsequent sections. At this density, friction dominates over activity, and proliferation is largely suppressed.

Fibroblast-myofibroblast monolayers exhibit nematic order. Steric interactions create aligned domains separated by disordered regions where topological defects, or regions of misalignment, emerge. In 2D, stable defects appear as either $+\frac{1}{2}$ defect, also known as a “comet” (Fig. 1b), or $-\frac{1}{2}$ defect, also known as a “trefoil” (Fig. 1c). Our goal is to identify the orientation field and track defect dynamics from microscopy videos. To end this, we first apply the structure tensor method [5], with the results shown as the yellow overlay (Fig. 1d). Then we identify defects using a topology-preserving algorithm [33], which automatically identifies the $\pm\frac{1}{2}$ defects, as illustrated in the insets of Fig. 1d. More details can be found in Section 4.5 and SI Section S5. Our analysis integrates prior works to suit our specific datasets. We modify the structure tensor method from Ref. [5], originally developed for phase-contrast microscopy, to work with fluorescence microscopy, because myofibroblasts are relatively flat and therefore exhibit poor contrast in phase contrast mode. We also extend the defect-detecting algorithm from Ref. [33], originally developed for microtubule networks, to cellular data by accounting for the greater discretization errors, and the resulting lower effective resolution, that arise from the larger size of the cells. Finally, we link the defect positions across frames using a particle-tracking scheme, originally developed in Ref. [34], which yields the full defect trajectories, from which the defect velocities can be computed.

2.2 Defect relaxation dynamics

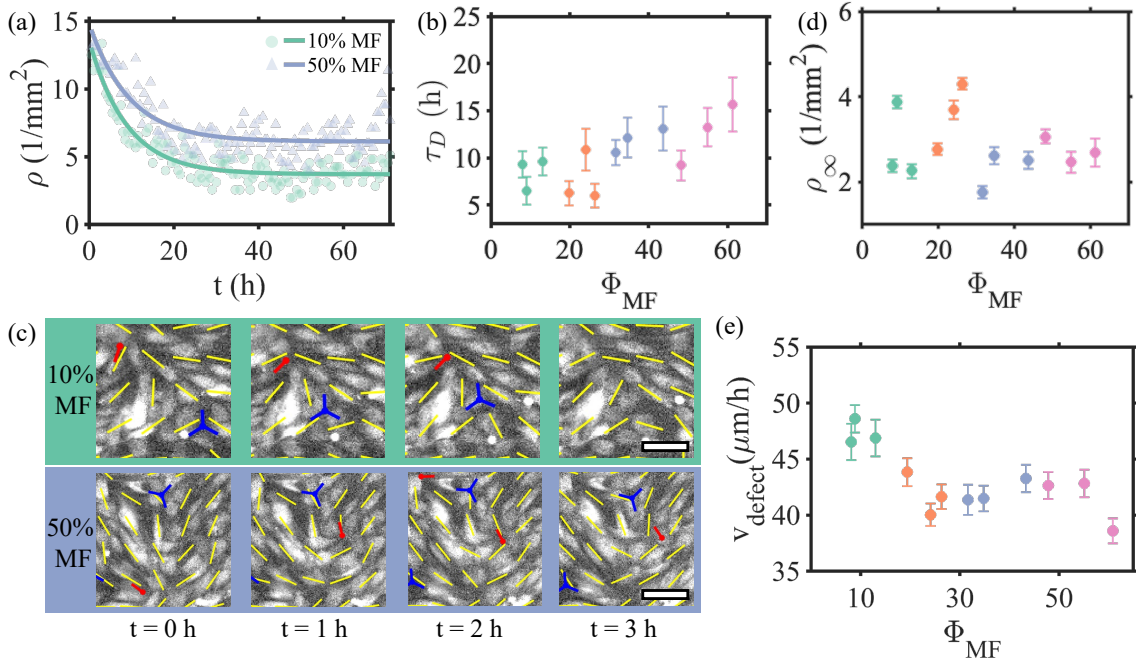


Figure 2: (a) The density of topological defects decreases over time and eventually plateaus at a finite value. Solid lines indicate the exponential fit. (b) Dependence of the decay constant (τ_D) on myofibroblast concentration Φ_{MF} . (c) Time sequence images showing the annihilation of defect pairs with opposite topological charges in both low and high concentrations of myofibroblasts. The scale bars are $100 \mu\text{m}$. (d) Dependence of steady-state defect density (ρ_∞) on myofibroblast concentrations Φ_{MF} . (e) The average velocity of all defects (v_{defect}) across myofibroblast concentrations Φ_{MF} .

We observe that the total number of both types of defects ρ decreases over time (Fig. 2a), and eventually reaches a plateau, $\rho \approx 2 \text{ mm}^{-2}$, comparable to earlier observations [35]. For different myofibroblast concentration, we plot the defect density ρ over time t (additional plots can be found in Fig. S6), and fit an exponential decay:

$$\rho(t) = (\rho_0 - \rho_\infty)e^{-t/\tau_D} + \rho_\infty, \quad (1)$$

where τ_D and ρ_∞ are the decay constant and steady-state defect numbers, respectively. Monolayers with different compositions of the two phenotypes exhibit distinct dynamics. We find that τ_D increases for monolayers with increasing Φ_{MF} (Fig. 2b). Correspondingly, we also find that defect recombination occurs notably more slowly in myofibroblast–fibroblast mixtures with increasing Φ_{MF} (Fig. 2c). In contrast, the plateau defect density, ρ_∞ , remains unchanged (Fig. 2d). ρ_∞ is comparable to literature values [35], and is consistent with a system with low activity [36], where the dynamics are governed by passive elastic relaxation. We observe a slower relaxation, with an approximately 25% reduction in the average defect velocity, as myofibroblast concentration in the monolayer composition increases by about six-fold (Fig. 2e).

We find that the slowdown of the defect recombination dynamics persists even when myofibroblasts constitute the majority of the sample ($\Phi_{MF} > 50\%$). Although isolated myofibroblasts typically exhibit a more rounded morphology (Fig. S2), and active nematic behavior in myofibroblasts has not previously been reported, in this system, they become polarized in the presence of fibroblasts. Under these conditions, the two phenotypes co-migrate, collectively exhibiting local alignment and robust nematic order. Myofibroblasts contribute to the overall dynamics not only as potential sources of disorder but also as active constituents that shape the collective motion. Consequently, the monolayer should be analyzed as an integrated system, rather than as two distinct subpopulations, to fully capture the continuous steric and mechanical interactions between the two phenotypes.

One useful framework to interpret these findings is active nematics with quenched disorder [37, 38]. In such systems, random field disorder partitions the material into uncorrelated domains and hinders the kinetics of structural reorganization [37]. Unlike boundary-induced cues, these perturbations are intrinsic and mobile within the system. As the disorder strength increases, both defect recombination dynamics and long-range order are suppressed. In this system, myofibroblasts act as the source of disorder, and increasing myofibroblast concentration increases the disorder strength.

Both cell velocities and defect velocities decrease with increasing myofibroblast concentration (SI, Fig. S4). Notably, topological defects often move much faster than the surrounding material, as their motion is governed by the system’s energy landscape and structural configuration rather than by bulk material transport. Moreover, despite the reduction in average speed, velocity correlations change only minimally with increasing myofibroblast concentrations, implying that structural relaxation dominates over cellular activity. This observation is consistent with a recent computational study [39] that reported that velocity correlations are less sensitive to the strength of quenched noise. Furthermore, the study predicts that the director texture becomes arrested while the flow persists, exhibiting long-range correlations and facilitating material transport. To our knowledge, our system represents the first experimental realization of a dry active nematic system with quenched disorder.

2.3 Alignment with an uniaxial imposed orientation

Surface topography can impose strong orientational guidance on fibroblasts and myofibroblasts through contact guidance [40–42]. One study directly compared the sensitivity of fibroblasts versus myofibroblasts to the dimension of topographic features, but the comparison was carried out for individual cells [42]. Does increasing Φ_{MF} in the monolayer also impede its ability to align with the imposed orientation?

The two phenotypes are premixed at various Φ_{MF} and seeded onto the substrates that are mechanically rubbed with sandpaper to establish directional cues (Fig. 3a). The cells were seeded at $\rho_{cell} \approx 750 \text{ mm}^{-1}$, and then fixed after 96 hours. Cell alignment is characterized by the 2D order parameter $S = \langle 2\cos^2\theta - 1 \rangle$, where θ denotes the deviation of the cell angle extracted from the preferred orientation (denoted by the double-sided arrow, Fig. 3b). The order parameter S decreases from around 0.6 to around 0.3 as the Φ_{MF} increases from 10% to 70%. The slowdown in defect recombination dynamics similarly leads to a decrease in S when cells are seeded on a unidirectionally oriented substrate. Additionally, we plot the fluctuation of angular distributions $P(\delta\theta)$ in Fig. 3c. Consistent with what is predicted in Ref. [37], the $P(\delta\theta)$ broadens with increasing Φ_{MF} , reaffirming myofibroblasts’ role as the source of quenched disorder in our system, which acts to inhibit reorganization. These observations also reveal that myofibroblasts are less responsive to external organizational cues, which may contribute to their role in the formation of disfiguring scars, by preventing the system from reaching an ordered or functional state. The rubbed substrate also serves as a visual and accessible platform for monitoring the progression of fibrotic disease.

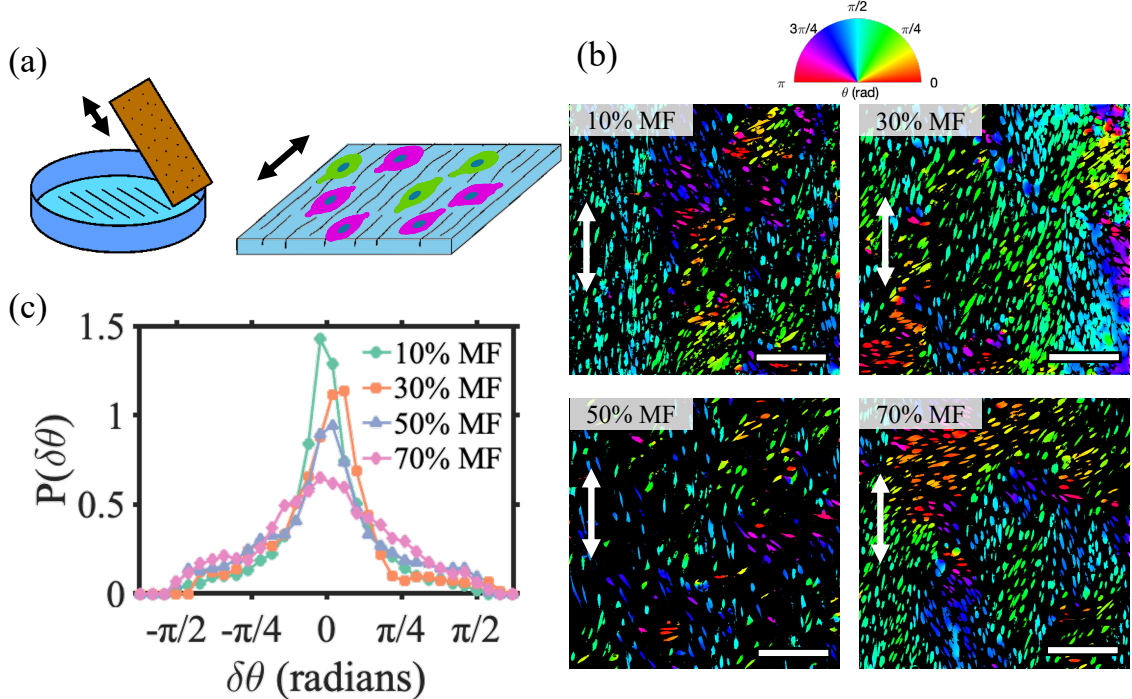


Figure 3: (a) Schematic of the rubbing protocol used to align cells, with cells orienting along the rubbing direction (denoted by double-sided arrows). (b) Polar distribution of director field angles. (c) Distribution of variation angle $\delta\theta$. (d) Spatial correlation of the nematic order parameter, where the color denotes the orientation angle, illustrated by the color wheel (above). The scale bars are 500 μm .

2.4 Different phenotypes develop different affinities to different defects

To understand why higher myofibroblast levels impede organization in monolayers, we compare defect locations with myofibroblast-rich regions. For consistency, we focus on a monolayer with $\Phi_{\text{MF}} \approx 50\%$ myofibroblast. Fluorescent channels were segmented using CellPose [43], and the densities of each phenotype are shown in Fig. 4a,b. Overlaying these densities with defects (Fig. 4c) reveals that myofibroblast-rich regions (green) coincide more with $-\frac{1}{2}$ defects (blue), while fibroblast-rich regions (magenta) coincide more with $+\frac{1}{2}$ defects (red). To assess whether this trend is general, we present cumulative statistics showing the preference for positively or negatively charged defects for each phenotype in Fig. 4, tallied from $n = 211$ defects using a custom algorithm (details of the code and the benchmarking procedures are provided in SI Section S7). Our analysis (Fig. 4d) indicates that myofibroblasts preferentially collocate with negatively charged $-\frac{1}{2}$ defects (61% of the time), whereas fibroblasts tend to associate with positively charged $+\frac{1}{2}$ defects (63% of the time).

We hypothesize that the defect dynamics presented in Fig. 2 are highly correlated with their compositions. Defects with charge $+\frac{1}{2}$ can self-propel whereas defects with charge $-\frac{1}{2}$ are often more stagnant [4, 35, 44, 45]. The velocity field extracted by PIV shows $+\frac{1}{2}$ defects tend to move faster (Fig. 4e, yellow regions). Further analysis reveals that regions in the vicinity of $-\frac{1}{2}$ defects travel at statistically significantly lower velocities compared with those surrounding $+\frac{1}{2}$ defects (Fig. 4f). Thus, it appears that myofibroblasts slow down global reorganization dynamics through their association with the slower-moving $-\frac{1}{2}$ defects. Previous studies showed that $+\frac{1}{2}$ defects tend to migrate [36] and accumulate [46] within regions or phases of higher activity. In our system, the fibroblast microphase corresponds to the high-activity region, characterized by increased motility, and they coincide with $+\frac{1}{2}$ defects. In contrast, the myofibroblast microphase exhibits slower dynamics, and tends to coincide with $-\frac{1}{2}$ defects. This is consistent with a system exhibiting increased friction [47] and reduced motility, hallmarks of the myofibroblast phenotype.

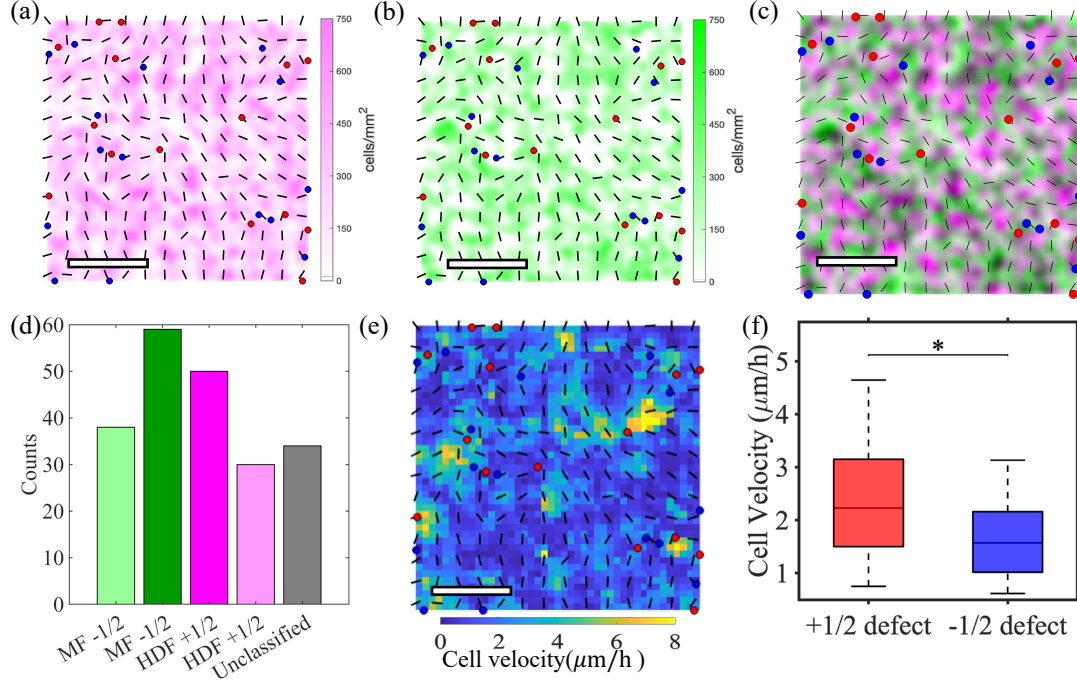


Figure 4: (a-b) Cell number density for (a) fibroblasts and (b) myofibroblasts. (c) Combined density plot for fibroblasts (magenta) and myofibroblasts (green). (d) Counts of fibroblasts and myofibroblast-enriched regions that coincide with $\pm \frac{1}{2}$ defects ($n = 202$ defects). (e) Spatial velocity map obtained from particle image velocimetry. (f) Box and whisker plots of velocities at $\pm \frac{1}{2}$ defect sites (from $n_{+1/2} = 15$ defects and $n_{-1/2} = 15$ defects, $p = 0.038$). The scale bars are 500 μm in panels (a-c) and (e).

2.5 Defect pinning on LCE fiber substrates

Mobile defects discussed so far move at substantial speeds (~ 10 s of $\mu\text{m}/\text{h}$), making cell-defect interactions challenging to follow. Therefore, lastly, we turn to pinned defects, which cannot relax or move. As discussed so far, we find that the mixture of fibroblasts and myofibroblasts can align with the imposed orientation, and their spatial arrangement is influenced by the mechanical forces and the distinct affinities of each cell type for different defects.

We achieve defect pinning by creating liquid crystal elastomer (LCE) fiber patterns of topological charge $\pm \frac{1}{2}$ following procedures in Refs. [14, 41] (Fig. 5a,b, more details can be found in Materials and Methods), coating them with collagen, and seeding them with a $\Phi_{\text{MF}} \approx 50\%$ mixtures. The HDF were prestained with CellTracker (magenta). After 24 hours, the cells are fixed and stained with DAPI (nuclei, blue) and Phalloidin (actin, green), as shown in the first column 1 in Fig. 5. We used a method similar to that described in the previous section to visualize the density map, as shown in the second column in Fig. 5. Then we compute the local density of myofibroblasts ϕ_{MF} , by counting the number of fibroblasts and myofibroblasts, within every annulus at an increment of $\Delta r = 30 \mu\text{m}$ from the center of the defect $|\mathbf{r} - \mathbf{r}_{\text{defect}}|$. For comparison, we approximate the myofibroblast concentration Φ_{MF} of the sample (dashed lines) by calculating its number density over the entire field of view, shown as the dotted lines in the third column. We find that, similar to mobile defects, $+\frac{1}{2}$ defects serve as sites where myofibroblasts concentrate, whereas $-\frac{1}{2}$ defects exhibit an excess of fibroblasts. These trends persist over distances exceeding 200 μm , well beyond the defect core of the fiber pattern. The presence of isolated, pinned defects with distinct cell-type selectivity supports the observed dynamics of defect movement. We next postulate the mechanism underlying this relative enrichment compared to the bulk.

Defects, as sites of strong distortion and stress concentration, also correlate with rare events such as apoptosis [12] and proliferation [3]. In particular, positively charged defects are associated with local compressive stresses that can promote cell extrusion, apoptosis, and morphogenesis [3, 48, 49]. Our previous work [50] demonstrates that fibroblasts and myofibroblasts differentially interpret stiffness heterogeneity, with myofibroblasts exhibiting greater sensitivity to stiffness gradients and generating stronger

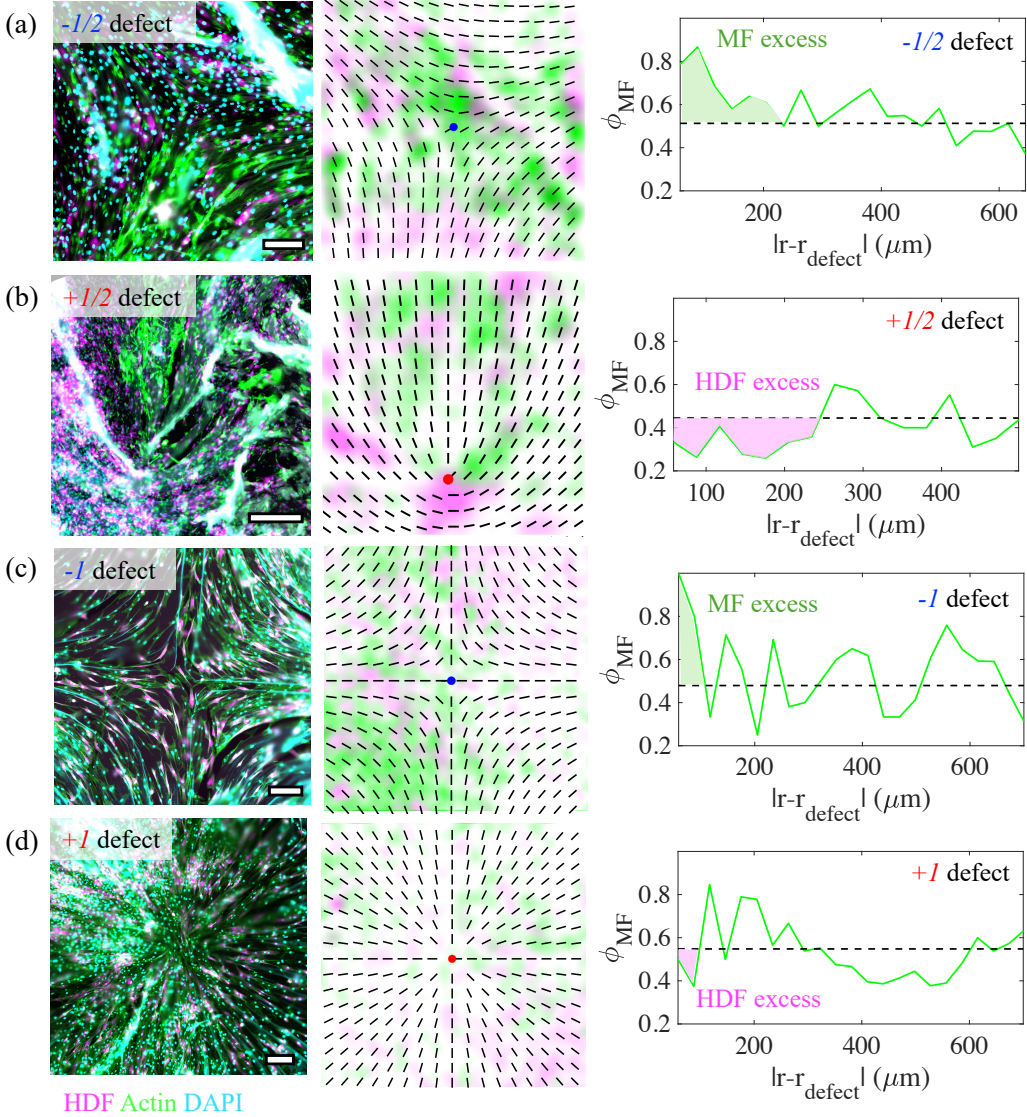


Figure 5: Cells cultured on LCE fibers with patterns of topological charges (a) $+\frac{1}{2}$, (b) $-\frac{1}{2}$, (c) $+1$, and (b) -1 . Column 1 shows the merged fluorescent micrographs with HDF (magenta), actin (green), and nuclei (blue). The scale bars are $200 \mu\text{m}$. Column 2 shows the cell density map overlaid with the underlying director field and the defects. Column 3 shows the local myofibroblast concentration ϕ_{MF} within an annulus at a distance $|\mathbf{r} - \mathbf{r}_{\text{defect}}|$ from the center of the defect. The dashed lines denote the sample average of myofibroblast concentration. The shaded area denotes the range where one phenotype is in excess near the defect core.

contractile forces in response to cell-scale features. Here, we find that cells with differentiated mechanical forces can also exhibit differentiated affinity for these sites. We hypothesize that, because myofibroblasts are highly contractile, they may also be excluded from the compressive $+\frac{1}{2}$ defect sites. If so, we would also expect myofibroblasts to be enriched at negatively charged defects and depleted at positively charged defects of higher charge. Therefore, we examine whether integer defects (± 1) preferentially recruit specific cell types. Since ± 1 defects spontaneously split into lower charges in 2D, we do not observe them on featureless substrates. Nonetheless, we may pattern integer defects using LCE fiber substrates (Fig. 5c,d) in the same manner, as defects of integer charges can sometimes appear at physiological or pathological settings, such as the tumor-stromal interface [51], or the optical nerve ending [52].

We observe a clear excess of myofibroblasts near the core of -1 defect (Fig. 5c), and a mild excess of fibroblasts near the radial $+1$ defect (Fig. 5d), consistent with $\pm \frac{1}{2}$ defects. Potential factors obscuring

the signals may stem from the splitting of higher-charged defects within the mixed-cell monolayer due to finite anchoring at the cell-LCE interface, which have been discussed in Ref. [53]. While the precise split distance of the mixed phenotypes is unknown, it can be approximated using the value for a pure HDF layer, where an integer defect typically separates into pairs spaced 200 to 500 μm apart [53]. Instead of a single defect, two nearby defects may each modulate the local density while simultaneously interacting with each other. Nonetheless, when we repeat this experiment with slightly different initial Φ_{MF} , we confirm that myofibroblasts are enriched in negatively charged defects and fibroblasts are enriched in positively charged defects in several other cases (Fig. S8).

Why do myofibroblasts favor negatively charged defects, while avoiding positively charged ones? The clue may lie in the type of stress near defects, modulated by factors including the rate of cell division [54]. An important mediator of nuclear responses is Yes-associated protein (YAP), an apoptosis inhibitor and downstream transducer of the Hippo signaling cascade. YAP functions as a cellular barometer for sensing local crowding [55]. YAP preferentially localizes to the nuclei (i.e., becomes activated) at sites of negatively charged defects [3, 12] and becomes deactivated at high cell densities [56] through a process known as contact-inhibited proliferation [57]. Consistent with these observations, we find that myofibroblasts exhibit elevated YAP activity near the core of $-\frac{1}{2}$ defects (Fig. S9). While myofibroblasts tend to have more activated YAP even when they are isolated [50], recent work indicates that, in the cell collective, density-dependent responses override substrate stiffness and other single-cell-level attributes in governing YAP activation [58].

These observations suggest two non-exclusive possibilities: myofibroblasts' intrinsically high YAP activation may cause them to preferentially occupy extensile sites, or conversely, myofibroblasts may preferentially localize to these sites to maintain YAP activation. On the one hand, characteristic patterns of motion, traction, and stress appeared long before defect formation [59]. This suggests that defects originate from pre-existing, coordinated cell-force and motility patterns, consistent with our observation that incorporating myofibroblasts slows down the defect recombination. On the other hand, our previous study [56] showed that collectively, cells can generate extensile internal stress to offset the effect of contact-inhibited proliferation, leading to reduced deactivation of YAP. Similarly, myofibroblasts may exploit persisting negatively charged defects by preferentially populating regions with extensile stress (-1 and $-\frac{1}{2}$ defects) to evade apoptosis. Myofibroblasts and defect perpetuate one another, establishing a feedback loop, consistent with the progressive and ultimately irreversible nature of fibrotic disease.

3 Discussion

Skin cell arrangement is far from random; the basket-weave pattern of the dermis serves as a shield for deeper layers. Under inflammatory conditions, the pattern is lost [32]. While extensive studies have characterized the steady-state properties of cellular assemblies of various degrees of order, time-resolved, large-scale studies of defects and their role in governing collective dynamics remain scarce. In this study, we aim to derive a self-organization rule governing the myofibroblast–fibroblast mixture, in order to uncover the functional implications of their spatial arrangement. We resort to understanding this phenotype-specific restructuring in 2D monolayers at high density, where collective dynamics emerge. Unlike previous studies on the biochemical and phenotypic responses of individual cells, we seek to elucidate how composition influences the emergent behavior, through large-scale live-cell microscopy of cell monolayers with an increasing fraction of myofibroblasts, mimicking fibrosis progression *in vitro*.

A multitude of studies [5, 12, 35] report the biological functions of defects, which are topologically and mechanically distinct from the surrounding tissues. Overall, in this system, we observe the emergence of robust nematic order in the broad range of myofibroblast concentration studied. In such dense 2D systems, $\pm\frac{1}{2}$ defects spontaneously appear, and oppositely charged defects recombine over time. By using an analytical method that conserves topological defect charges, we track movements and densities of defects over time. We observe that higher Φ_{MF} leads to reduced defect recombination rates, while the steady-state defect density remains largely unaffected. The former indicates that the slowed defect dynamics are likely due to the downregulated motility of myofibroblasts compared to fibroblasts. The latter suggests that, over long timescales, equilibrium defect densities reflect similar overall activity across different systems. Despite the reduction in the magnitude of the velocity of both the defect and the cells with increasing Φ_{MF} , we find that the spatial velocity correlations remain similarly long-ranged, over hundreds of μm , across all Φ_{MF} . These observations echo recent theoretical studies of quenched nematics

[37–39] where the source of disorder is mobile and intrinsic.

We show that the slowed dynamics of defect recombination hinder the myofibroblasts from achieving well-ordered alignment under the externally imposed, unidirectional alignment. The reduced ability to maintain uniform alignment is reflected in a more spread-out distribution of angle deviations from the preferred direction. We thereby establish means to examine the collective behavior of a dense monolayer, providing a straightforward way to quantitatively distinguish the progression of fibrotic disease.

Depending on their signs, $\pm \frac{1}{2}$ defects often exhibit distinct characteristics. Positively-charged, $+\frac{1}{2}$ defects are highly mobile [4, 5] and primarily responsible for driving recombination dynamics. They also tend to be confined within regions of high activity [36, 46]. Similarly, while $-\frac{1}{2}$ defects can be easily immobilized by the pillars, $+\frac{1}{2}$ defects remain motile in an active nematic composed of motile bacteria [60]. It is known that cells with distinct contractile and extensile forces self-sort based on the nature of their forces [4, 61]. In this work, we find that cells with distinct forces also respond differently to different mechanical stresses at topological defects. Our analysis reveals that myofibroblasts have an affinity to $-\frac{1}{2}$ defects while the fibroblasts tend to localize at $+\frac{1}{2}$ defects. Myofibroblasts, with their upregulated contractility, appear to sort themselves away from compressive $+\frac{1}{2}$ defects. The depletion of myofibroblasts from the more active $+\frac{1}{2}$ defect sites is also consistent with the slowdown of the overall recombination dynamics of the monolayer as Φ_{MF} increases. We find that this phenotype-selective mechanism at the defect core applies even to pinned defects and those with higher charges.

Recent work suggests that myofibroblasts are often primed for apoptosis but remain viable due to anti-apoptotic factors [30, 62]. Beyond biochemical factors, our findings indicate that mechanical forces associated with topological defects may also influence downstream protein expressions through an outside-in process. We find that, consistent with previous studies, the apoptosis inhibitor YAP is deactivated near positively charged defects [12] but remains active near negatively charged defects [3]. The preferential localization of myofibroblasts near negatively charged defects suggests a feedback loop in which myofibroblasts prolong the lifespan of topological defects and then leverage these same defects to promote their own survival. These effects are emergent and arise collectively from the interaction between the phenotypes. While persistent myofibroblast activation likely arises from a myriad of biochemical and mechanical factors, this study sheds light on an underexplored route and suggests that targeting myofibroblasts at specific sites could produce a compounding effect.

On the experimental front, we demonstrate that myofibroblasts not only stabilize defects but also potentially exploit these sites to evade apoptosis. The local mechanical environment may play a key role in supporting their survival by offsetting density-induced compressive stress. On the theoretical front, the observed behavior is reminiscent of recent theoretical works on active nematics with quenched disordered [37, 38], where the magnitude of disorder slows down defect recombination dynamics, while flow persists [39]. To our knowledge, this work is the first study to demonstrate behaviors of quenched disorder in a biologically relevant system. We hope this work motivates further experimental studies on the interplay between cell phenotype and topological defects, as well as complementary theoretical and simulation investigations into defect dynamics in quenched nematics.

4 Materials and Methods

4.1 Materials

All chemicals were purchased from Sigma-Aldrich (St. Louis, MO), and used without modification unless otherwise stated. Azodye SD1 dye was purchased from DIC Corporation (Tokyo, Japan). Reactive monomer RM257 was purchased from Ambeed (Arlington Heights, IL), and a mixture of small molecule liquid crystal mixture was purchased from Instec Inc (Boulder, CO, catalog no. LC-VATS14). Dulbecco's Modified Eagle's Medium (DMEM), DMEM F12 Medium, fetal bovine serum (FBS), phosphate-buffered saline (PBS), Bovine Serum Albumin (BSA), 100x antibiotic-antimycotic, and 100x penicillin-streptomycin (pen-strep) were purchased from Gibco (Grand Island, NY). Transforming growth factor-beta 1 (TGF- β 1, ab50036), FITC anti-alpha smooth muscle actin antibody (ab8211), and phalloidin-iFluor 555 (ab176756) were purchased from Abcam (Cambridge, United Kingdom). Hoechst 33342, 16 wt% paraformaldehyde solution (PFA), CellTracker in Deep Red (C34565) and Green (C7025) were purchased from ThermoFisher (Waltham, MA). Primary anti-rabbit YAP (NB110-58358) was purchased

from Novus Biologicals (Centennial, CO). The secondary antibody Alexa Fluor 488 AffiniPure Goat Anti-Rabbit IgG (AB2338052) was purchased from Jackson ImmunoResearch Inc (West Grove, PA). Water was dispensed from a Milli-Q system with resistivity = 18.2 MΩ·cm at 25°C.

4.2 Cell acquisition, culturing, and treatments

Adult human dermal fibroblast (HDFa) cells were purchased from the American Type Culture Collection (ATCC, Manassas, VA, catalog no. PCS-201-012). HDFs were maintained at 37°C with 5% CO₂ in complete media composed of DMEM, supplemented with 10 vol% FBS, and 1x pen-strep. The media was refreshed every 2 days, and the cells were sub-cultured upon reaching 70-80% confluency. Fibroblasts were labeled by CellTracker Deep Red.

Early passages (P<5) were used for induction. To induce the myofibroblast phenotype in vitro, we first cultured HDFA to confluence, and then grew them in serum-starved media for 24 hours. Cells were rinsed with PBS, and incubated in serum-free media with 10 ng/ml TGF-β1 for 96 hours. After 48 hours, cell media was refreshed, and fresh TGF-β1 was added. Myofibroblasts were labeled by CellTracker Green.

4.3 Live cell microscopy

The 4-well glass-bottom Petri dishes (35 mm, Cellvis, Mountain View, CA, catalog D35C4-20-0-N, #1.5 cover glass) were pre-coated with a low-concentration collagen solution and rinsed 3x with PBS. Cells were seeded at $\rho_{\text{cell}} \approx 750 \text{ mm}^{-1}$ density. Live cell imaging began as soon as the cells had attached to the bottom of the dish (approximately 6 hours after seeding). Cells were maintained in onstage incubators at 37 °C under 5% CO₂, and imaged using a 10x air objective (NA = 0.8), 4x4 binning, acquired in both far red (peak wavelength = 602 nm) and green (peak wavelength = 517 nm), at a time interval of every 30 minutes. The pixel size is 2.344 μm . Approximately 100 frames were acquired for each Φ_{MF} . Tens of images were stitched together following procedures in [10] using an automated stage and the ZEN software (Carl Zeiss AG, Germany).

4.4 Immunofluorescence

Prior to observation, cells were fixed using a 4 wt% PFA, and stained with antibodies and fluorescent markers. Actin and nuclei were stained by Phalloidin-iFluor 555 (1000× dilution) and Hoechst 33342 (1 $\mu\text{g}/\text{mL}$) following standard protocols [10]. YAP staining was performed as described in Refs. [56, 63].

4.5 Defect identification

Details of the analysis can be found in SI Section S5. Briefly, raw phase contrast or fluorescence microscopy images were preprocessed to enhance cellular features. Cell orientation fields were calculated using the structure tensor method, by applying a Gaussian smoothing ($\sigma = 9.4 \mu\text{m}$ or 4 pixels) filter to 32 pixel \times 32 pixel windows ($75 \mu\text{m} \times 75 \mu\text{m}$). Defect detection was implemented by adopting the algorithm from [33] by identifying patch regions of grid points undergoing rapid rotation ($\Delta\theta > \frac{\pi}{4}$) of the director field. The topological charge for each patch was computed from ($s = \frac{\oint \Delta\theta}{2\pi}$), summed along the path of the loop. This way, topological charges are conserved.

4.6 Fabrication of LCE fiber substrates with different topological charges

Glass slides (AmScope, Irvine, CA) were thoroughly cleaned with detergent in an ultrasonic bath for 8 minutes and then rinsed with water, acetone, and isopropanol. After drying in the oven at 80°C for 10 minutes to evaporate solvents, they were further cleaned with a plasma cleaner (Harrick Plasma, Ithaca, NY) for 5 minutes. The fibers were prepared by a projection display based on procedures detailed in [41]. Briefly, a solution of azodye SD1 dye at 0.2 wt % in N,N-dimethylformamide (DMF) was evenly deposited on the glass slide by spin coating at 3000 rpm for 30 sec, and annealed at 120 °C for 15 min. Two such coated glass slides were assembled into a chamber with coated sides facing each other, separated by spacer beads (Cospheric, Somis, CA, diameter $2a = 20 \mu\text{m}$). Then, patterns were generated using a rotating linear polarizer in front of the projection display. A solution of 7 wt% reactive monomer RM257, 92 wt% LC mixture, and 1 wt% photoinitiator was introduced into the chamber at isotropic temperature (120°C) and slowly cooled down to the nematic phase. The sample was cured under UV light with power 6 mW/cm² at 365 nm wavelength for 1 h to crosslink the reactive monomer completely. Afterward, the

samples were immersed in hexane overnight to wash away the uncrosslinked small-molecule LC. Finally, the samples were dipped in liquid nitrogen for a few seconds and split with a razor blade.

Acknowledgements

The authors thank Toshi Parmar, Jacob Notbohm, and Cristina Marchetti for stimulating discussions about active nematics. We acknowledge Kyogo Kawaguchi and Kevin Mitchell for sharing the codes for determining director-field orientation and for identifying topological defects, Shervin Issakhani for initial code development, Valerie Horsley and Elizabeth Caves for providing the healthy and SSc cells from donors, and for the helpful discussion on fibrotic markers and media conditions, and Nick Bernardo for assistance with machining the imaging stage.

Funding

This work is partially supported by the National Science Foundation under the Grant OAC-2411044.

Author contributions

Yimin L designed the project. Yuxin L, JC, and ZZ performed experiments. ZZ and Yimin L performed numerical analysis. All authors have contributed to the writing of the manuscript and approved the final version of the manuscript.

Conflicts of interest

The authors declare no conflicts of interest.

Data availability statement

The data collected and the analysis codes generated for this study will be made available through a permanent GitHub repository upon acceptance of the manuscript.

References

- [1] Gordon T Stewart. Liquid crystals in biology i. historical, biological and medical aspects. *Liq. Cryst.*, 30(5):541–557, 2003.
- [2] Gordon T Stewart. Liquid crystals in biology ii. origins and processes of life. *Liq. Cryst.*, 31(4):443–471, 2004.
- [3] Kirsten D Endresen, MinSu Kim, Matthew Pittman, Yun Chen, and Francesca Serra. Topological defects of integer charge in cell monolayers. *Soft Matter*, 17(24):5878–5887, 2021.
- [4] Lakshmi Balasubramaniam, Amin Doostmohammadi, Thuan Beng Saw, Gautham Hari Narayana Sankara Narayana, Romain Mueller, Tien Dang, Minnah Thomas, Shafali Gupta, Surabhi Sonam, Alpha S Yap, Yusuke Toyama, René-Marc Mège, Julia M. Yeomans, and Benoît Ladoux. Investigating the nature of active forces in tissues reveals how contractile cells can form extensile monolayers. *Nat. Mater.*, 20(8):1156–1166, 2021.
- [5] Kyogo Kawaguchi, Ryoichiro Kageyama, and Masaki Sano. Topological defects control collective dynamics in neural progenitor cell cultures. *Nature*, 545(7654):327–331, 2017.
- [6] V Yashunsky, DJG Pearce, C Blanch-Mercader, F Ascione, Pascal Silberzan, and L Giomi. Chiral edge current in nematic cell monolayers. *Phys. Rev. X*, 12(4):041017, 2022.
- [7] Nathan D Bade, Randall D Kamien, Richard K Assoian, and Kathleen J Stebe. Edges impose planar alignment in nematic monolayers by directing cell elongation and enhancing migration. *Soft Matter*, 14(33):6867–6874, 2018.

- [8] Guillaume Duclos, Simon Garcia, HG Yevick, and P Silberzan. Perfect nematic order in confined monolayers of spindle-shaped cells. *Soft Matter*, 10(14):2346–2353, 2014.
- [9] Aniruddh Murali, Prasoon Awasthi, Kirsten Endresen, Arkadiusz Goszczak, and Francesca Serra. Splay and bend deformations in cells near corners. *Soft Matter*, 2025.
- [10] Yimin Luo, Mengyang Gu, Minwook Park, Xinyi Fang, Younghoon Kwon, Juan Manuel Urueña, Javier Read de Alaniz, Matthew E Helgeson, Cristina M Marchetti, and Megan T Valentine. Molecular-scale substrate anisotropy, crowding and division drive collective behaviours in cell monolayers. *J. R. Soc. Interface*, 20(204):20230160, 2023.
- [11] Toshi Parmar, Fridtjof Brauns, Yimin Luo, and M. Cristina Marchetti. Proliferating nematic that collectively senses an anisotropic substrate. *PRX Life*, pages –, Dec 2025.
- [12] Thuan Beng Saw, Amin Doostmohammadi, Vincent Nier, Leyla Kocgozlu, Sumesh Thampi, Yusuke Toyama, Philippe Marcq, Chwee Teck Lim, Julia M Yeomans, and Benoit Ladoux. Topological defects in epithelia govern cell death and extrusion. *Nature*, 544(7649):212–216, 2017.
- [13] Lakshmi Balasubramaniam, René-Marc Mège, and Benoît Ladoux. Active nematics across scales from cytoskeleton organization to tissue morphogenesis. *Current Opinion in Genetics & Development*, 73:101897, 2022.
- [14] Junrou Huang, Juan Chen, and Yimin Luo. Cell-sheet shape transformation by internally-driven, oriented forces. *Adv. Mater.*, page 10.1002/adma.202416624, 2025.
- [15] Guillaume Duclos, Christoph Erlenkämper, Jean-François Joanny, and Pascal Silberzan. Topological defects in confined populations of spindle-shaped cells. *Nat. Phys.*, 13(1):58–62, 2017.
- [16] Yonit Maroudas-Sacks, Liora Garion, Lital Shani-Zerbib, Anton Livshits, Erez Braun, and Kinneret Keren. Topological defects in the nematic order of actin fibres as organization centres of hydra morphogenesis. *Nat. Phys.*, 17(2):251–259, 2021.
- [17] Amin Doostmohammadi and Benoit Ladoux. Physics of liquid crystals in cell biology. *Trends Cell Biol.*, 2021.
- [18] Daniele Martella, Lorenzo Pattelli, Camilla Matassini, Francesca Ridi, Massimo Bonini, Paolo Paoli, Piero Baglioni, Diederik S Wiersma, and Camilla Parmeggiani. Liquid crystal-induced myoblast alignment. *Adv. Healthc. Mater.*, 8(3):1801489, 2019.
- [19] Guillaume Duclos, Carles Blanch-Mercader, Victor Yashunsky, Guillaume Salbreux, Jean-François Joanny, Jacques Prost, and Pascal Silberzan. Spontaneous shear flow in confined cellular nematics. *Nat. Phys.*, 14(7):728–732, 2018.
- [20] Ekta Makhija, Yang Zheng, Jiahao Wang, Han Ren Leong, Rashidah Binte Othman, Ee Xien Ng, Eng Hin Lee, Lisa Tucker Kellogg, Yie Hou Lee, Hanry Yu, Zhiyong Poon, and Krystyn J. Van Vliet. Topological defects in self-assembled patterns of mesenchymal stromal cells in vitro are predictive attributes of condensation and chondrogenesis. *Plos one*, 19(3):e0297769, 2024.
- [21] Jiachen Zhang, Yubing Guo, Wenqi Hu, Ren Hao Soon, Zoey S Davidson, and Metin Sitti. Liquid crystal elastomer-based magnetic composite films for reconfigurable shape-morphing soft miniature machines. *Adv. Mater.*, 33(8):2006191, 2021.
- [22] Cécile Jacques, Joseph Ackermann, Samuel Bell, Clément Hallopeau, Carlos Perez Gonzalez, Lakshmi Balasubramaniam, Xavier Trepot, Benoît Ladoux, Ananya Maitra, Raphael Voituriez, and Danijela Matic Vignjevic. Aging and freezing of active nematic dynamics of cancer-associated fibroblasts by fibronectin matrix remodeling. *bioRxiv*, pages 2023–11, 2023.
- [23] Anna E Argento, Maria L Varela, Gurveer Singh, Daiana P Visnuk, Binyamin Jacobovitz, Mary E Rutherford, Marta B Edwards, Quentin Chaboche, Daniel A Orringer, Jason A Heth, Maria G. Castro, Daniel A. Beller, Carles Blanch-Mercader, and Lowenstein Pedro R. Three-dimensional topological defects and quasi-long-range order in biological liquid crystals. *bioRxiv*, 2025.
- [24] Pedro R Lowenstein. Oncostreams organize peritumoral glioma infiltration: Metastasis. *Nat. Cancer*, pages 1–3, 2025.
- [25] Nuria E Cabrera-Benitez, Matteo Parotto, Martin Post, Bing Han, Peter M Spieth, Wei-Erh Cheng, Francisco Valladares, Jesus Villar, Mingayo Liu, Masaaki Sato, Haibo Zhang, and Arthur S Slutsky.

Mechanical stress induces lung fibrosis by epithelial-mesenchymal transition (emt). *Crit. Care Med.*, 40(2):510, 2012.

[26] Pierre-Jean Wipff, Daniel B Rifkin, Jean-Jacques Meister, and Boris Hinz. Myofibroblast contraction activates latent tgf- β 1 from the extracellular matrix. *J. Cell Biol.*, 179(6):1311–1323, 2007.

[27] Mohammadreza Pakyari, Ali Farrokhi, Mohsen Khosravi Maharlooie, and Aziz Ghahary. Critical role of transforming growth factor beta in different phases of wound healing. *Advances in wound care*, 2(5):215–224, 2013.

[28] Pernille Juhl, Sandie Bondesen, Clare Louise Hawkins, Morten Asser Karsdal, Anne-Christine Bay-Jensen, Michael Jonathan Davies, and Anne Sofie Siebuhr. Dermal fibroblasts have different extracellular matrix profiles induced by tgf- β , pdgf and il-6 in a model for skin fibrosis. *Sci. Rep.*, 10(1):17300, 2020.

[29] James J Tomasek, Giulio Gabbiani, Boris Hinz, Christine Chaponnier, and Robert A Brown. Myofibroblasts and mechano-regulation of connective tissue remodelling. *Nature reviews Molecular cell biology*, 3(5):349–363, 2002.

[30] Boris Hinz and David Lagares. Evasion of apoptosis by myofibroblasts: a hallmark of fibrotic diseases. *Nature Reviews Rheumatology*, 16(1):11–31, 2020.

[31] Shuying Yang, Fernando R Valencia, Benedikt Sabass, and Sergey V Plotnikov. Quantitative analysis of myofibroblast contraction by traction force microscopy. In *Myofibroblasts: Methods and Protocols*, pages 181–195. Springer, 2021.

[32] A Ishida-Yamamoto. The basket-weave pattern is present in the skin for a reason. *British Journal of Dermatology*, 182(2), 2020.

[33] Amanda J Tan, Eric Roberts, Spencer A Smith, Ulyses Alvarado Olvera, Jorge Arteaga, Sam Fortini, Kevin A Mitchell, and Linda S Hirst. Topological chaos in active nematics. *Nat. Phys.*, 15(10):1033–1039, 2019.

[34] John C Crocker and David G Grier. Methods of digital video microscopy for colloidal studies. *J. Colloid Interface Sci.*, 179(1):298–310, 1996.

[35] Trinish Sarkar, Victor Yashunsky, Louis Brézin, Carles Blanch Mercader, Thibault Aryaksama, Mathilde Lacroix, Thomas Risler, Jean-François Joanny, and Pascal Silberzan. Crisscross multilayering of cell sheets. *PNAS nexus*, 2(3):pgad034, 2023.

[36] Rui Zhang, Steven A. Redford, Paul V. Ruijgrok, Nitin Kumar, Ali Mozaffari, Sasha Zemsky, Aaron R. Dinner, Vincenzo Vitelli, Zev Bryant, Margaret L. Gardel, and Juan J. de Pablo. Spatiotemporal control of liquid crystal structure and dynamics through activity patterning. *Nat. Mater.*, 20(6):875–882, 2021.

[37] Sameer Kumar and Shradha Mishra. Active nematics with quenched disorder. *Phys. Rev. E*, 102(5):052609, 2020.

[38] Sameer Kumar and Shradha Mishra. Active nematic gel with quenched disorder. *Phys. Rev. E*, 106(4):044603, 2022.

[39] Yutaka Kinoshita and Nariya Uchida. Active nematic liquid crystals under a quenched random field. *Europhys. Lett.*, 151(5):57002, 2025.

[40] Greta Babakhanova, Jess Krieger, Bing-Xiang Li, Taras Turiv, Min-Ho Kim, and Oleg D Lavrentovich. Cell alignment by smectic liquid crystal elastomer coatings with nanogrooves. *J. Biomed. Mater. Res. Part A*, 108(5):1223–1230, 2020.

[41] Juan Chen, Oluwafemi Isaac Akomolafe, Netra Prasad Dhakal, Mahesh Pujiyam, Omar Skalli, Jinghua Jiang, and Chenhui Peng. Nematic templated complex nanofiber structures by projection display. *ACS Applied Materials & Interfaces*, 14(5):7230–7240, 2022.

[42] Simon A Pot, Sara J Liliensiek, Katheren E Myrna, Ellison Bentley, James V Jester, Paul F Nealey, and Christopher J Murphy. Nanoscale topography-induced modulation of fundamental cell behaviors of rabbit corneal keratocytes, fibroblasts, and myofibroblasts. *Invest. Ophthalmol. Vis. Sci.*, 51(3):1373–1381, 2010.

[43] Carsen Stringer, Tim Wang, Michalis Michaelos, and Marius Pachitariu. Cellpose: a generalist algorithm for cellular segmentation. *Nat. Methods*, 18(1):100–106, 2021.

[44] Guillaume Duclos, Raymond Adkins, Debarghya Banerjee, Matthew SE Peterson, Minu Varghese, Itamar Kolvin, Arvind Baskaran, Robert A Pelcovits, Thomas R Powers, Aparna Baskaran, Federico Toschi, Michael F. Hagan, Sebastian J. Streichan, Vincenzo Vitelli, Daniel A. Beller, and Zvonimir Dogic. Topological structure and dynamics of three-dimensional active nematics. *Science*, 367(6482):1120–1124, 2020.

[45] Luca Giomi, Mark J Bowick, Prashant Mishra, Rastko Sknepnek, and M Cristina Marchetti. Defect dynamics in active nematics. *Philosophical Transactions of the Royal Society A: Mathematical, Physical and Engineering Sciences*, 372(2029):20130365, 2014.

[46] KVS Chaithanya, Aleksandra Ardaševa, Oliver J Meacock, William M Durham, Sumesh P Thampi, and Amin Doostmohammadi. Transport of topological defects in a biphasic mixture of active and passive nematic fluids. *Commun. Phys.*, 7(1):302, 2024.

[47] Amin Doostmohammadi, Jordi Ignés-Mullol, Julia M Yeomans, and Francesc Sagués. Active nematics. *Nat. Comm.*, 9(1):1–13, 2018.

[48] Yonit Maroudas-Sacks and Kinneret Keren. Mechanical patterning in animal morphogenesis. *Annu. Rev. Cell Dev. Biol.*, 37:469–493, 2021.

[49] Pau Guillamat, Carles Blanch-Mercader, Guillaume Pernollet, Karsten Kruse, and Aurélien Roux. Integer topological defects organize stresses driving tissue morphogenesis. *Nat. Mater.*, 21(5):588–597, 2022.

[50] Yuxin Luo and Yimin Luo. Rigidity sensing of inclusions directs differentiated cell elongation and force generation across phenotypes. *ACS Biomater. Sci. Eng.*, 2025.

[51] Paolo P Provenzano, Kevin W Eliceiri, Jay M Campbell, David R Inman, John G White, and Patricia J Keely. Collagen reorganization at the tumor-stromal interface facilitates local invasion. *BMC medicine*, 4(1):38, 2006.

[52] Yamil Miranda-Negrón and José E García-Arrarás. Radial glia and radial glia-like cells: Their role in neurogenesis and regeneration. *Frontiers in Neuroscience*, 16:1006037, 2022.

[53] Taras Turiv, Jess Krieger, Greta Babakhanova, Hao Yu, Sergij V Shiyanovskii, Qi-Huo Wei, Min-Ho Kim, and Oleg D Lavrentovich. Topology control of human fibroblast cells monolayer by liquid crystal elastomer. *Sci. Adv.*, 6(20):eaaz6485, 2020.

[54] Kurmanbek Kaiyrbekov, Kirsten Endresen, Kyle Sullivan, Zhaofei Zheng, Yun Chen, Francesca Serra, and Brian A Camley. Migration and division in cell monolayers on substrates with topological defects. *Proc. Natl. Acad. Sci. U.S.A.*, 120(30):e2301197120, 2023.

[55] Tito Panciera, Luca Azzolin, Michelangelo Cordenonsi, and Stefano Piccolo. Mechanobiology of yap and taz in physiology and disease. *Nature reviews Molecular cell biology*, 18(12):758–770, 2017.

[56] Juan Chen and Yimin Luo. Disodium cromoglycate templates anisotropic short-chain peg hydrogels. *ACS Appl. Mater. Interfaces*, 16(26):33223–33234, 2024.

[57] Mariana Pavel, Maurizio Renna, So Jung Park, Fiona M. Menzies, Thomas Ricketts, Jens Füllgrabe, Avraham Ashkenazi, Rebecca A. Frake, Alejandro Carnicer Lombarte, Carla F. Bento, Kristian Franze, and David C. Rubinsztein. Contact inhibition controls cell survival and proliferation via yap/taz-autophagy axis. *Nat. Comm.*, 9(1):2961, 2018.

[58] Valeria Grudtsyna, Vinay Swaminathan, and Amin Doostmohammadi. Packing-driven mechanotransduction: local crowding overrides adhesion and stiffness cues for yap activation in cellular collectives. *bioRxiv*, pages 2025–10, 2025.

[59] Pradip K Bera, Molly McCord, Jun Zhang, and Jacob Notbohm. Traction and stress control formation and motion of $1/2$ topological defects in epithelial cell monolayers. *Newton*, 1(8), 2025.

[60] Nuris Figueroa-Morales, Mikhail M Genkin, Andrey Sokolov, and Igor S Aranson. Non-symmetric pinning of topological defects in living liquid crystals. *Commun. Phys.*, 5(1):301, 2022.

- [61] Preeti Sahu, Daniel M Sussman, Matthias Rübsam, Aaron F Mertz, Valerie Horsley, Eric R Dufresne, Carien M Niessen, M Cristina Marchetti, M Lisa Manning, and Jen M Schwarz. Small-scale demixing in confluent biological tissues. *Soft Matter*, 16(13):3325–3337, 2020.
- [62] David Lagares, Alba Santos, Paula E. Grasberger, Fei Liu, Clemens K. Probst, Rod A. Rahimi, Norihiko Sakai, Tobias Kuehl, Jeremy Ryan, Patrick Bhola, Joan Montero, Mohit Kapoor, Murray Baron, Xaralabos Varelas, Daniel J. Tschumperlin, Anthony Letai, and Andrew M. Tager. Targeted apoptosis of myofibroblasts with the bh3 mimetic abt-263 reverses established fibrosis. *Sci. Transl. Med.*, 9(420):eaal3765, 2017.
- [63] Arupratan Das, Robert S Fischer, Duoqia Pan, and Clare M Waterman. Yap nuclear localization in the absence of cell-cell contact is mediated by a filamentous actin-dependent, myosin ii-and phospho-yap-independent pathway during extracellular matrix mechanosensing. *J. Biol. Chem.*, 291(12):6096–6110, 2016.